A Multimodal Evaluation of Transcranial Photobiomodulation in Mild Cognitive Impairment: Cognitive, Metabolic, and Neuroimaging Outcomes of a Pilot Randomized Control Trial

Neda Rashidi-Ranjbar[1], Nathan Churchill[1], Mirjana Jerkic[1], Reza Zomorrodi[2], Ori Rotstein[1,3], Raphael Schneider[1,4], Ana C. Andreazza[5,6], Tarek K. Rajji[2,7], Simon J Graham[8,9], David G Munoz[1,10], Luis Fornazzari[1], Lew Lim[11], Tom A. Schweizer[1,12], Corinne E Fischer*[1,5]

1. Keenan Research Centre for Biomedical Science, Li Ka Shing Knowledge Institute, St. Michael's Hospital, Toronto, ON, Canada.
2. Temerty Centre for Therapeutic Brain Intervention, Centre for Addiction and Mental Health, Toronto, Ontario, Canada
3. Temerty Faculty of Medicine, Department of Surgery, University of Toronto, Toronto, ON, Canada.
4. Temerty Faculty of Medicine, Division of Neurology, University of Toronto, Toronto, ON, Canada.
5. Temerty Faculty of Medicine, Department of Psychiatry, University of Toronto, Toronto, ON, Canada.
6. Department of Pharmacology & Toxicology, Mitochondrial Innovation Initiative, University of Toronto, Toronto, ON, Canada
7. Department of Psychiatry, UT Southwestern Medical Center, Dallas, Texas
8. Department of Medical Biophysics, University of Toronto, Toronto, Ontario, Canada.
9. Physical Sciences Platform, Sunnybrook Research Institute, Sunnybrook Health Sciences Centre, Toronto, ON, Canada.
10. Temerty Faculty of Medicine, Department of Laboratory Medicine and Pathobiology, University of Toronto, Toronto, ON, Canada.
11. Vielight Inc, Toronto, ON, Canada
12. Temerty Faculty of Medicine, Department of Neurosurgery, University of Toronto, Toronto, ON, Canada

Abstract 300 words.

INTRODUCTION

Mild cognitive impairment (MCI), a prodromal stage of Alzheimer's disease and related dementias (ADRD), offers a critical window for early intervention. Mitochondrial dysfunction is increasingly recognized as a driver of neurodegeneration, yet most therapies target downstream protein aggregation. Transcranial photobiomodulation (tPBM)—delivery of near-infrared (NIR)

light to stimulate mitochondrial respiration—offers a non-invasive, metabolism-based therapeutic strategy.

METHODS

In a single-blinded, randomized, sham-controlled pilot trial (NCT05563298), we evaluated the safety, feasibility, and biological effects of home-based tPBM in individuals aged ≥50 with MCI. Participants received either active (n = 10) or sham (n = 10) treatment using visually identical NIR devices targeting default mode network regions and the olfactory bulb. Active devices emitted pulsed 810 nm light for 20 minutes per session, six days per week for six weeks; sham devices emitted light for only 2 seconds per session. No serious adverse events occurred; three mild-to-moderate events were reported, and adherence exceeded 98%.

RESULTS

Active tPBM led to greater improvements in global cognition, as measured by the Mini-Mental State Examination, and in episodic memory, as measured by the delayed recognition test of the California Verbal Learning Test–Second Edition. Blood analyses showed increased serum pyruvate and lactate, a reduced lactate-to-pyruvate ratio, and lower plasma IL-6. Neuroimaging revealed enhanced default mode network connectivity and focal cortical volume and thickness gains.

DISCUSSION

These data demonstrate safety, preliminary efficacy, and support future definitive clinical studies.

Background

Alzheimer's disease (AD) and related dementias (ADRD) affect over 55 million individuals worldwide, with approximately 10 million new cases annually, posing immense social and economic burdens[1]. By the time clinical symptoms emerge, extensive synaptic loss and neuronal death have already occurred, limiting the efficacy of existing therapies[2]. Recently approved anti-amyloid agents, such as lecanemab, provide modest clinical benefit in early AD[3], and their use is constrained by high costs, infrastructure requirements (e.g., PET imaging, infusion protocols), and the risk of adverse events such as amyloid-related imaging abnormalities[4].

Importantly, up to 45% of dementia cases may be preventable through early intervention[5,6]. This underscores the urgent need for scalable, noninvasive strategies, particularly in high-risk populations such as those with mild cognitive impairment (MCI). The aim is to stabilize or improve cognitive function during this critical window of disease modification.

MCI involves measurable cognitive decline, typically in episodic memory, without major functional impairment[7]. Approximately 15% of individuals with MCI progress to dementia within two years, and one-third convert to AD within five years[7]. Mitochondrial dysfunction is increasingly recognized as an early feature of AD[8]. Cortical neurons are highly energy-dependent, making them vulnerable to impaired oxidative phosphorylation[9]. Studies in MCI show reduced cytochrome-c oxidase activity, lower ATP production, and elevated reactive oxygen species[10–12,13], contributing to redox imbalance and accelerating amyloid and tau pathology[14,15]. Nonetheless, most therapies continue to focus on amyloid, tau, or inflammation[16], while mitochondria-directed approaches remain scarce—highlighting the need for more effective interventions that address mitochondrial dysfunction.

Transcranial photobiomodulation (tPBM) is a noninvasive neuromodulatory approach that delivers near-infrared (NIR) light (~700-1100 nm) to stimulate cytochrome-c-oxidase (CCO) and enhance mitochondrial respiration in cortical tissue[17]. NIR light wavelengths align with the CCO absorption peak[18], facilitating efficient photon capture. tPBM has been shown to increase ATP production, reduce ROS, and promote nitric oxide release[19–21]. In AD mouse models (e.g., 5×FAD, APP/PS1), repeated tPBM reduces Aβ burden, preserves synaptic integrity, and improves memory performance[22–24]. Preliminary human studies using tPBM in individuals with MCI[25] or AD[26,27], have reported improvements in attention, executive function, memory, regional cerebral blood flow[25], and default mode network (DMN) functional connectivity[27]. However, these studies are limited in number and often lack rigorous design elements such as sham controls and adequate sample sizes[25-29].

To address these limitations, we conducted a single-blinded, randomized, sham-controlled feasibility trial of tPBM in individuals with MCI (n = 20; https://www.clinicaltrials.gov/study/NCT05563298). The primary endpoint was change in cognitive function—including global cognition, episodic memory, and processing speed—from

baseline to post-intervention (week 7). Secondary endpoints focused on investigating potential mechanisms of action, including biomarkers of mitochondrial function (serum lactate, pyruvate, and the lactate/pyruvate ratio[62]), neurometabolite ratios in the posterior cingulate cortex (PCC)—a key hub of the DMN and one of the earliest regions to show metabolic decline in MCI and AD[28,29]—as well as DMN functional connectivity and cerebral blood flow. Exploratory measures included blood-based biomarkers of neurodegeneration and neuroinflammation, structural MRI indices of brain atrophy, neuropsychiatric symptoms, and sleep quality. By integrating clinical, cognitive, blood-based biomarker, and imaging outcomes, this pilot trial aimed to assess feasibility and safety, evaluate preliminary efficacy, and explore mechanistic pathways to inform future large-scale randomized trials of tPBM for early cognitive decline.

Methods

Participants and Study Design

Between March 2023 and December 2024, we enrolled twenty community-dwelling adults aged 60–85 years who met the 2011 NIA–AA clinical criteria for MCI due to Alzheimer's disease (NCT05563298). This criteria is based on clinical assessment, without biomarker confirmation[63].

Candidates were referred from the St. Michael's Hospital Memory Clinic or responded to community advertisements. A single geriatric psychiatrist screened every participant in the Memory Clinic. All cognitive tests, blood draws, and MRI scans were carried out at St. Michael's Hospital. Written informed consent was obtained under a protocol approved by the St. Michael's Hospital Research Ethics Board. Inclusion criteria: a subjective cognitive concern (self, informant, or clinician); MoCA score 19–25 with memory impairment; CDR 0.5 with preserved activities of daily living; and at least eighth-grade education. Exclusion criteria: any contraindication to MRI or venipuncture; current psychiatric or other neurological disease; uncontrolled systemic illness; history of stroke or seizures; scalp photosensitivity; use of major anticoagulants; significant functional impairment (CDR ≥ 1.0); or inability to provide informed consent.

Sample Size

This feasibility-focused pilot trial included 10 participants per group, consistent with methodological recommendations for pilot studies aimed at estimating key parameters to inform the design of a subsequent definitive trial powered to detect medium-to-large effect sizes[64].

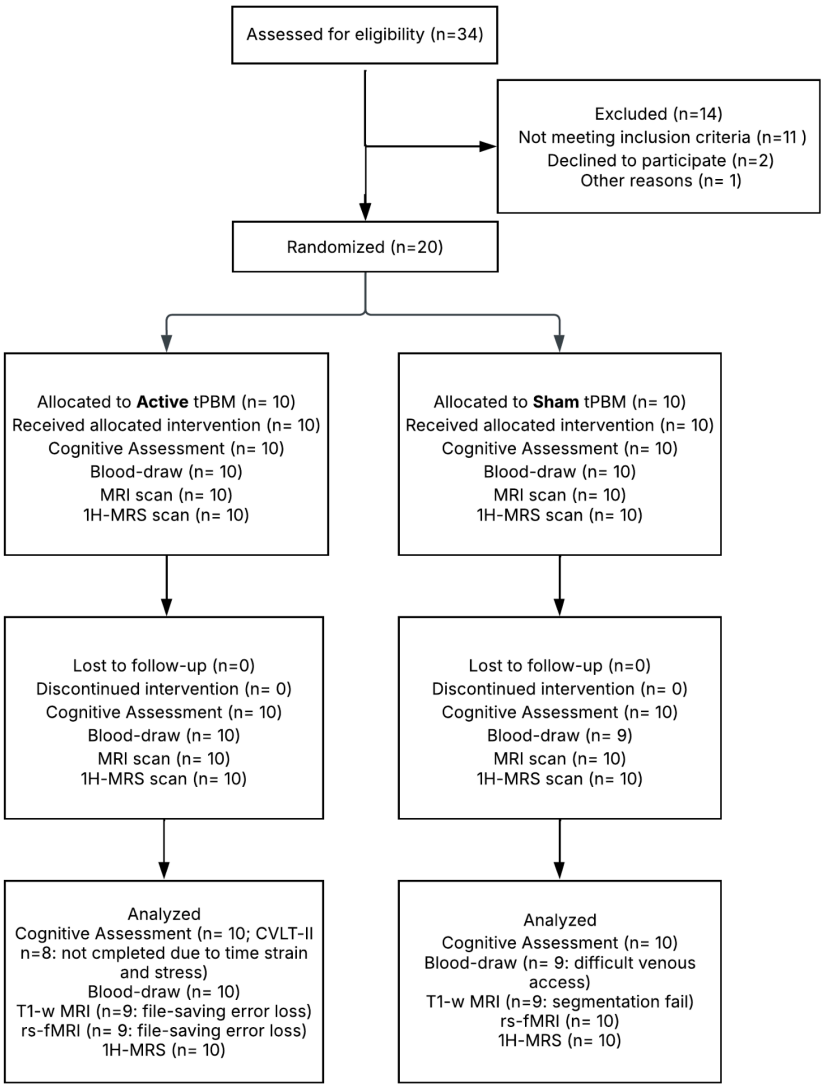

Figure 7. Participant flow diagram, including numbers assessed for eligibility, enrolled, and analyzed.

Study Design

Following screening, all twenty participants were randomized (1:1) to active tPBM or sham via a computer-generated block sequence (block size = 4). Randomization lacked third-party concealment, however, participants remained fully blinded to their treatment assignment

throughout the duration of the study. A single research coordinator handled every aspect of the trial—screening, enrollment, randomization, weekly check-in calls, and outcome assessments—and therefore was necessarily unblinded. Participants themselves remained unaware of their assigned condition (active vs. sham), making this a single-blind study.

Intervention

Each participant received a portable Class II research-use-only device (Health Canada ITA #347303) equipped with five near-infrared LEDs (810 nm) targeting DMN hub regions: one frontal LED targeting the medial prefrontal cortex (positioned along the midline at the hairline), one posterior LED targeting the posterior cingulate cortex (placed at the crown of the head), and two lateral LEDs targeting the bilateral temporal/angular regions (which aligned naturally with the headset design). An additional intranasal LED, targeting the olfactory bulb, was inserted into the nostril through which the participant reported easier breathing (Figure 6). In the active group, when turned on, the frontal LED delivered 75 mW/cm², each posterior/temporal LED delivered 100 mW/cm², and the intranasal LED delivered 25 mW/cm²; all were pulsed at 40 Hz with a 50 % duty cycle. Heat generation was minimal (< 0.5 °C). The sham device was identical in appearance and emitted NIR light only for the first two seconds of each twenty-minute session, then powered off for the remainder. Both active and sham units produced the same audible beep if dislodged, preserving participant blinding. All devices complied with Class II Health Canada safety requirements.

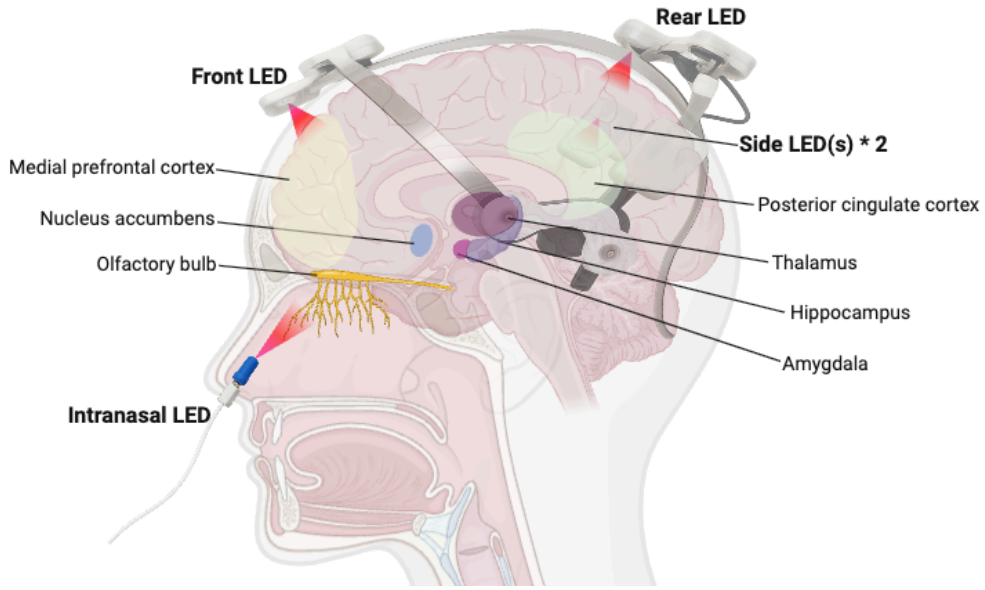

Figure 7. Schematic of the Transcranial photobiomodulation (tPBM) headset and projected light paths illustrates the five LED emitters used in the present study. Red cones depict the approximate spread of five LED emitters. The frontal LED, positioned at the front hairline, targets the medial prefrontal cortex; the posterior LED on the crown illuminates the posterior cingulate cortex; the two lateral LEDs (only one visible in this view) fall naturally into position without manual adjustment, covering the temporo-parietal cortices; and an intranasal LED, inserted in the nostril, reaches the olfactory bulb and adjacent ventral forebrain. Subcortical structures are highlighted for reference. Illustration created with BioRender.com.

Device Training

At baseline, the research coordinator provided a thirty-minute, in-person training session on device placement (scalp landmarks), cleaning, and diary completion.

Home-Based Treatment and Monitoring

Participants completed 20-minute home sessions six days a week for six weeks (36 sessions total). Adherence and safety were tracked through (1) participant diaries, (2) weekly calls from the study coordinator, and (3) an adverse-event log.

During each call, the coordinator: a) verified the number of sessions completed, b) resolved any technical problems, and 3) documented side effects or safety concerns.

Compliance was defined a priori as ≥30 of 36 sessions (≈ 83 %).

Primary Outcomes

Cognitive Function Assessments (n = 10 active, n = 10 sham)

Cognitive assessments were conducted at baseline and following the six-week intervention (week 7) by the same coordinator, who was trained in psychometric testing. In a fixed order to minimize variability, participants completed the Mini-Mental State Examination (MMSE)[66] was used to assess global cognition, with total scores serving as the primary outcome measures. The Trail Making Test (TMT)[67] Parts A and B recorded completion times in seconds as primary outcomes, reflecting processing speed (Part A) and executive set-shifting ability (Part B). The

TMT B/A ratio was also calculated to account for individual differences in processing speed and more specifically isolate executive control. Verbal learning and memory were assessed using the California Verbal Learning Test–Second Edition (CVLT-II)[68], administered using the Standard Form at baseline and the Alternate Form at week 7 to minimize practice effects. Primary outcomes for the CVLT-II included total recall across the five learning trials (Trials 1–5), twenty-minute delayed free recall, and long-delay recognition hits, capturing verbal learning, long-term memory, and recognition memory, respectively. The CVLT-II was selected for its sensitivity to episodic memory decline in MCI [69] (Kramer et al., 2020). We used the standard/alternate form pairing, which offers acceptable reliability (r = 0.61–0.73) and minimizes practice effects (Cohen's *d* = –0.01 to 0.18), making it suitable for longitudinal designs [70]. Two participants in the active group did not complete the post-intervention CVLT-II assessment due to time constraints and reported stress associated with the task.

Secondary Outcomes

Sleep quality was assessed using the Pittsburgh Sleep Quality Index (PSQI)[71], with the global PSQI score as the primary outcome, where higher scores indicate poorer sleep quality.

Neuropsychiatric symptoms were evaluated using the Mild Behavioral Impairment Checklist (MBI-C)[72], with the total MBI-C severity score as the primary measure, capturing the overall burden of behavioral symptoms.

Blood-Based Biomarkers (n = 10 active, n = 9 sham)

Immediately following cognitive assessments, blood samples were collected at baseline and week 7 (post-intervention). Paired serum and plasma samples were available for 19 participants; one participant in the sham group was unable to complete the post-intervention blood draw due to difficult venous access.

Whole blood was drawn into two 10 mL vacutainer tubes—one containing K_2EDTA and one without anticoagulant, which was allowed to clot upright at room temperature for 30–45 minutes. EDTA and serum tubes were then centrifuged at 2000 x g for 25 minutes at room temperature or at 4°C, respectively (Sorvall ST16 Plus centrifuge, ThermoFisher Scientific, Markham, ON, Canada) using ClickSeal biocontainment lids.. Plasma and serum were aliquotted under sterile

conditions in a biosafety cabinet, inspected for turbidity, and re-centrifuged if needed. All aliquots were stored in cryovials at –80°C within two hours of collection.

Serum Metabolomics Analysis (n = 10 active, n = 9 sham)

NMR spectroscopy was used to quantify serum metabolites, with a primary focus on lactate and pyruvate as markers of mitochondrial function.

To remove high-molecular-weight proteins and lipoproteins, samples were deproteinized using 3 kDa cut-off centrifugal filters (Amicon Microcon YM-3), pre-rinsed to eliminate residual glycerol[73]. Samples were centrifuged at 10,000 rpm for 20 minutes, and filtrates were inspected for membrane integrity. If volumes were below 250 µL, 150 mM KH_2PO_4 buffer (pH 7.0) was added to reach 173.5 µL. A standard buffer (54% D_2O, 5.84 mM DSS, 5.84 mM 2-chloropyrimidine-5-carboxylate, 0.1% NaN_3) was then added (46.5 µL).

^1H-NMR spectra were acquired at 25°C using a Bruker Avance III 700 MHz spectrometer with a 5 mm HCN cryoprobe, applying the NOESY pre-saturation sequence (noesy1dpr) for quantitative accuracy[74]. The DSS methyl signal was used as an internal standard (0 ppm). Spectra were processed and quantified using an in-house version of MAGMET software[74,75], which fits known metabolite signatures from a custom database. All the serum samples were processed and analyzed by the Metabolomics Innovation Centre (TMIC) at the University of Alberta (https://metabolomicscentre.ca/service/nmr-analysis/), and results were reviewed by an expert NMR spectroscopist to ensure accuracy.

Plasma Biomarkers (n = 10 active, n = 9 sham)

Exploratory plasma markers of neuroinflammation (IL-1β, IL-10, IL-6, TNF-α)[76,77], neurodegeneration (GFAP, NfL)[78,79], tau pathology (phosphorylated tau-217)[80], and synaptic plasticity (BDNF)[81] were examined.

Plasma aliquots were thawed once and centrifuged at 10,000 × g for 10 minutes at 4°C, to remove any particles that might be present in the samples. Biomarker and cytokine concentrations (pg/mL) were measured using the Ella platform (ProteinSimple, Bio-Techne, New

York, USA), an automated microfluidic immunoassay system, with V5-generation single and multiplex cartridges. Assays followed the manufacturer's technical guidelines[82].

Phosphorylated tau-217 was measured separately using the Simoa® ALZpath p-Tau 217 assay (Quanterix).

Neuroimaging

Brain atrophy was evaluated separately using MRI-based measures of cortical thickness and subcortical volumes[80]**.**

Acquisition Parameters

Neuroimaging was conducted at baseline and week 7 using a 3T Siemens Skyra scanner with a 64-channel head coil. High-resolution structural imaging included a 3D T1-weighted Magnetization Prepared Rapid Acquisition Gradient Echo (MPRAGE) sequence (TI/TE/TR = 1100/4.37/2500 ms, flip angle = 7°, 192 sagittal slices, 256 × 256 matrix, 1.0 mm slice thickness, 1.0 × 1.0 mm in-plane resolution, 140 Hz/px bandwidth), and a 3D Fluid Attenuated Inversion Recovery (FLAIR) sequence (TI/TE/TR = 1600/388/5000 ms, 192 sagittal slices, 256 × 256 matrix, 1.0 mm slice thickness, 1.0 × 1.0 mm in-plane resolution, 751 Hz/px bandwidth).

Resting-state functional MRI (rs-fMRI) was acquired using 2D multi-slice T2*-weighted echo planar imaging (EPI; TE/TR = 30/2000 ms, flip angle = 70°, 36 oblique-axial slices, 200 × 200 mm field of view, 64 × 64 matrix, 3.5 mm slice thickness with 0.5 mm gap, 3.1 × 3.1 mm in-plane resolution, 2442 Hz/px bandwidth), producing 270 brain volumes (9 minutes total). Participants were instructed to lie still with eyes open and not focus on anything in particular.

Single-voxel proton magnetic resonance spectroscopy (^{1}H-MRS) was performed in the posterior cingulate cortex (voxel size = 20 × 20 × 20 mm^{3}) using a Point RESolved Spectroscopy (PRESS) sequence (TE/TR = 30/2000 ms, flip angle = 90°, 80 water-suppressed and 4 unsuppressed averages, 1024 points, 1200 Hz bandwidth).

Pseudo-continuous arterial spin labeling (PCASL) was acquired with TR/TE = 4930/36.8 ms, flip angle = 120°, 8 tag-control pairs, 1500 ms labeling duration, and 1800 ms post-labeling delay. Scans were acquired with 2.5 mm isotropic resolution over a 240 × 240 mm field of view,

using 48 slices and background suppression. A 3D turbo gradient spin-echo (TGSE) readout was used with 2-fold in-plane acceleration via GRAPPA (2480 Hz/px bandwidth). A calibration scan was also acquired using identical parameters but without tagging pulses or background suppression, and with a TR of 7000 ms.

One participant from the active group had their week 7 MRI scan lost due to a file-saving error; however, their MRS data were preserved and included in the analysis.

MRI Data Exclusion

Of the 20 enrolled participants, neuroimaging analyses were modality-specific due to data loss and quality control exclusions: One participant's structural and functional MRI data (T1 and rs-fMRI) was lost due to a file-saving error, though their ^{1}H-MRS data were unaffected and included. One additional participant's T1-weighted scan failed segmentation due to a pituitary adenoma and was excluded from structural analyses. One ASL scan was excluded because it was acquired with different parameters than the rest of the dataset.

rs-fMRI Processing (n = 9 active, n = 10 sham)

Resting-state fMRI data were processed using a hybrid pipeline that incorporated ANTs (http://stnava.github.io/ANTs), AFNI (https://afni.nimh.nih.gov), FSL (https://fsl.fmrib.ox.ac.uk/fsl), and custom in-house scripts. Full details of the acquisition and preprocessing procedure have been published previously[83]. Anatomical T1-weighted images were first skull-stripped, segmented, and non-linearly registered to the MNI152 template. First, volumes with framewise displacement > 0.5 mm were identified and removed, followed by slice-timing correction and motion correction. Functional images were then non-linearly normalized to MNI152 space and resampled to 3 mm isotropic resolution. Spatial smoothing was applied using a 6 mm full-width at half-maximum (FWHM) Gaussian kernel. Subsequent preprocessing steps included linear detrending, regression of six motion parameters, and removal of nuisance signals derived from white matter (WM) and cerebrospinal fluid (CSF) time series. We applied the Schaefer 200-parcel cortical atlas (Yeo's seven networks) [84] plus the Tian 16-region subcortical atlas (eighth network)[85] to extract mean time series from 216 ROIs. Fisher-z-transformed Pearson correlations were computed between all region of interest (ROI)

pairs, producing 216 × 216 connectivity matrices. Within-network connectivity was assessed as the mean z-value of all ROI pairs in a given network; between-network connectivity was assessed as the mean z-value between ROIs of two distinct networks.

Proton Magnetic Resonance Spectroscopy (1H-MRS) Processing (n = 10 active, n = 10 sham)

^{1}H-MRS spectra were fitted with TARQUIN v4.3.10 (https://tarquin.sourceforge.net). Spectra with Cramér–Rao Lower Bounds < 20% were retained; none were excluded. Metabolite concentrations (N-acetylaspartate [NAA], choline [Cho], myo-inositol [mI], and lactate [Lac]) were expressed as ratios to creatine (e.g., NAA/Cr, Lac/Cr).

T1-MPRAGE Imaging Processing (n = 9 active, n = 9 sham)

T1-weighted were processed with FreeSurfer (Longitudinal) v6.0 for cortical reconstruction and subcortical segmentation (hippocampus, amygdala, thalamus, caudate, putamen). All segmentations were visually inspected and, if necessary, manually corrected to ensure consistency. For each remaining participant, change scores (Δ = week 7 – baseline) were calculated for bilateral volumes of six subcortical bilateral (n = 12) regions using the "aseg" parcellation[86], and for bilateral cortical thickness across eighteen bilateral (n = 36) Desikan–Killiany regions [87,88] (n = 36; 18 bilateral regions).

CBF Processing (n = 9 active, n = 9 sham)

Pseudo-continuous arterial spin labeling (PCASL) data were processed using a custom pipeline that integrates in-house software with standard open-source packages, including including AFNI (https://afni.nimh.nih.gov), FSL (https://fsl.fmrib.ox.ac.uk/fsl), and ANTs (http://stnava.github.io/ANTs)[89]. Outlier volumes were identified and removed, and the remaining volumes were aligned to the corresponding M_0 calibration scan. Cerebral blood flow (CBF) maps were estimated in mL/100g/min using a kinetic model adapted from ASLtbx[90] with default parameters. The resulting CBF maps were normalized to MNI space, resampled to 3 mm isotropic resolution, and spatially smoothed using a 6 mm full-width at half-maximum (FWHM) Gaussian kernel. Next, we extracted mean CBF values extracted using the Yeo's 7-network cortical atlas ROIs to examine network-level perfusion in the active and sham groups.

In addition, group-level CBF comparison of the whole brain was conducted using permutation-based inference (*randomise* in FSL) with threshold-free cluster enhancement (TFCE)[91].

Statistical Analysis

Statistical analyses were performed in R v4.2.2. For each outcome, change scores (Δ = week 7 − baseline) were tested for normality using the Shapiro–Wilk test ($\alpha = 0.05$). Primary analyses focused on the between-group differences in change scores. Within-group, pre–post comparisons are reported in the Supplementary Information for descriptive purposes only. If both groups met normality, independent two-sample t-tests were used (with Welch's correction if variances were unequal), and effect sizes were expressed as Cohen's d. If normality was violated in either group, Mann–Whitney U tests were used with rank-biserial correlation ($r = Z/\sqrt{N}$) as the effect size. This analytic strategy was applied uniformly across cognitive, imaging, and biomarker outcomes. No correction for multiple comparisons was applied, given the hypothesis-generating nature and limited sample size of this pilot study. A priori hypotheses focused on core mitochondrial and network-level endpoints (e.g., lactate, pyruvate, lactate/pyruvate ratio, DMN connectivity), with other comparisons considered exploratory. Missing data were handled via pairwise deletion.

Results

Demographics

Participants were evenly split into active (n = 10) and sham (n = 10) groups. The mean age, sex distribution, and years of education did not differ significantly between the groups. Baseline MoCA scores were identical, confirming successful randomization.

Table 1. Demographic characteristics of the active and sham groups.

Variable	**Active**	**Sham**	**Statistics**

	n=10	n=10	
Age yrs. (mean ± sd)	69.5 ± 7.6	71.4 ± 6.3	t(18)=−0.6, p=0.55
N (%) Female	4 (40%)	6 (60%)	$\chi^2(1) = 0.8$, p = 0.37
Education Yrs. (mean ± sd)	16.0 ± 2.5	16.9 ± 3.6	t(18)=−0.6, p=0.52
MoCA baseline (mean ± sd)	23.9 ± 0.9	23.9 ± 1.9	t(18)=0, p=1.0

Compliance & Safety

Adherence was uniformly high: all active participants completed 35–36 of 36 sessions (mean = 98.9 ± 1.5 %), and all sham participants completed 35–36 sessions (mean = 98.8 ± 1.7 %). No serious adverse events occurred. In the active group, one participant reported a mild headache in week 6 and another transient mood disturbance in week 6; both events were *possibly related* to device use, as they resolved spontaneously after sessions ceased. In the sham group, one participant reported a self-limited headache during the second week, which resolved without treatment.

Cognitive function (n = 10 active, n = 10 sham; CVLT-II: n = 8 active, n = 10 sham)

tPBM improved memory on multiple measures: CVLT-II long-delay recognition hits increased by 1.38 ± 2.38 in the active treatment group versus a decline of –2.00 ± 3.55 in the sham group (t(18)=2.4, p=0.029, d=1.08), and long-delay cued recall was increased by +1.12 ±1.95 in the active group , compared to a decrease of –1.00 ± 2.30 in the sham group (t(18)=2.11, p=0.050, d=0.98). Global cognition (MMSE) likewise improved: active participants gained +1.00 ± 1.25 points versus a –0.50 ± 1.58 decline in sham (t(18)=2.36, p=0.035, d=1.05). Executive function (TMT-B) showed a trend favoring active treatment (–32.26 ± 38.04 vs. –4.11 ± 23.85 sec; t(18)=-1.98, p=0.065, d=-0.89). No significant changes were observed in processing speed (TMT-A), sleep quality (PSQI), or neuropsychiatric symptoms (MBI-C) (Figure 1).

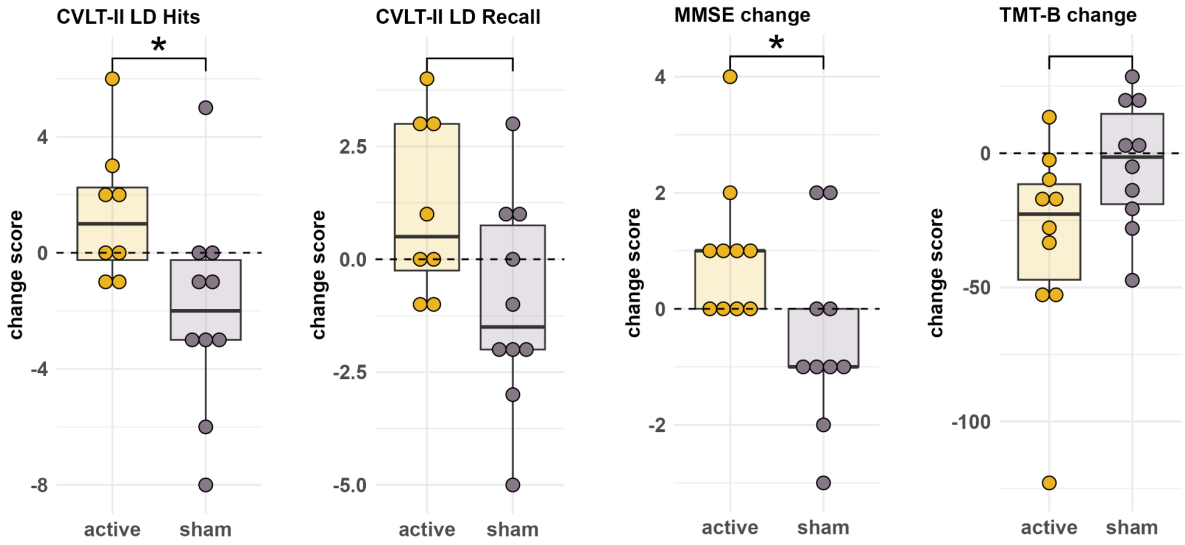

Figure 1. Cognitive Outcomes in Active vs. Sham Groups

Blood-Based Biomarkers (n = 10 active, n = 9 sham)

Serum Metabolomics

In the active group, serum pyruvate increased by +16.50 ± 28.44 µM compared to a decrease of –19.43 ± 23.09 µM in the sham group (t(18)=3.04, p=0.0075, d=1.38), and the lactate-to-pyruvate ratio decreased by –5.98 ± 12.58 versus an increase of +8.67 ± 7.95 in sham (t(18)=–3.06, p=0.0077, d=–1.37). Serum sarcosine increased by +0.05 ± 1.03 µM in active compared to +1.04 ± 0.89 µM in sham (t(18)=–2.24, p=0.038, d=–1.02), while serum urea decreased by –341.28 ± 585.56 mg/dL in active versus an increase of +360.19 ± 771.41 mg/dL in sham (t(18)=–2.21, p=0.042, d=–1.03). Serum L-carnitine increased by +0.96 ± 10.18 µM in active compared to a decrease of –9.18 ± 10.33 µM in sham (t(18)=2.15, p=0.046, d=0.99). Finally, serum L-alanine increased by +138.70 ± 195.82 µM in active versus a decrease of –8.94 ± 122.29 µM in sham (W=71, p=0.043, Z=2.04), and serum L-lactic acid increased by +417.70 ± 892.06 µM compared to a decrease of –183.56 ± 710.15 µM in sham (W=71, p=0.0350, Z=2.12) (Figure 2).

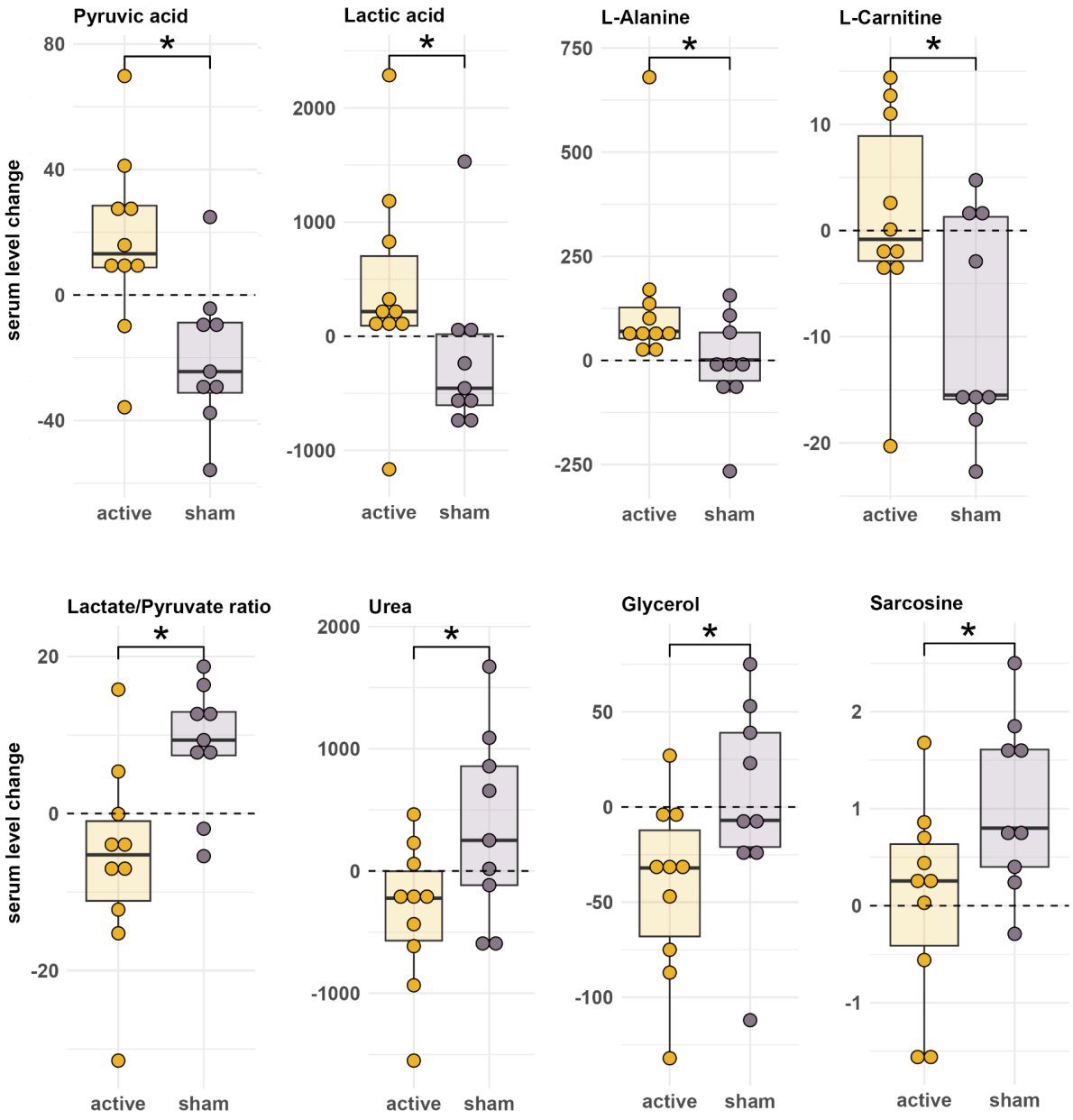

Figure 2. Changes in Serum Mitochondrial Metabolites and Related Biomarkers

Plasma Biomarkers

Plasma IL-6 declined by 1.50 ± 2.61 pg/mL in active versus increased by 0.27 ± 0.69 pg/mL in sham. Because active Δ violated normality (Shapiro–Wilk $p < 0.01$), a Wilcoxon test confirmed a

significant reduction in IL-6 with active tPBM (W = 17.5, Z = –2.24, p = 0.027, r = –0.52). No other plasma markers differed between groups (Figure 3).

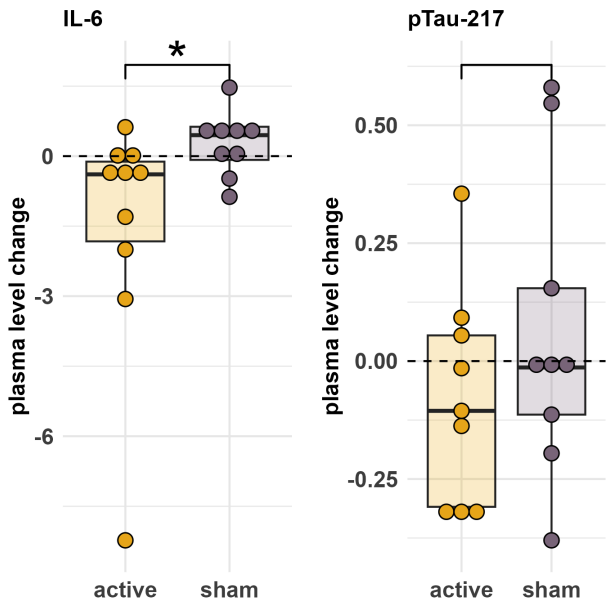

Figure 3. Changes in Plasma Inflammatory Marker in Response to tPBM

Neuroimaging

rs-fMRI (n = 9 active, n = 10 sham)

Active tPBM increased default-mode network functional connectivity (FC) (Δ = +0.077 ± 0.126) compared with a decrease in sham (Δ = –0.095 ± 0.148; t(18) = 2.73, p = 0.014, Cohen's d = 1.25). Similarly, FC between caudate–DMN increased by 0.057 ± 0.161 in active versus –0.135 ± 0.166 in sham (t(18) = 2.55, p = 0.021, d = 1.17). In contrast, within-network FC of the limbic network decreased by –0.149 ± 0.249 in active but increased by 0.209 ± 0.079 in sham (t(18) = –2.15, p = 0.048, d = –0.99). No other network differences reached significance (Figure 4a).

1H-MRS (n = 10 active, n = 10 sham)

In the posterior cingulate cortex (PCC), total N-acetylaspartate to creatine ratio (tNAA/Cr) in the PCC trended higher in active (Δ = +0.230 ± 0.748) versus sham (Δ = –0.091 ± 0.285; Wilcoxon

W = 74, p = 0.075, r = 0.18; n = 10 per group). No other ¹H-MRS metabolites differed between or within groups (Figure 4b).

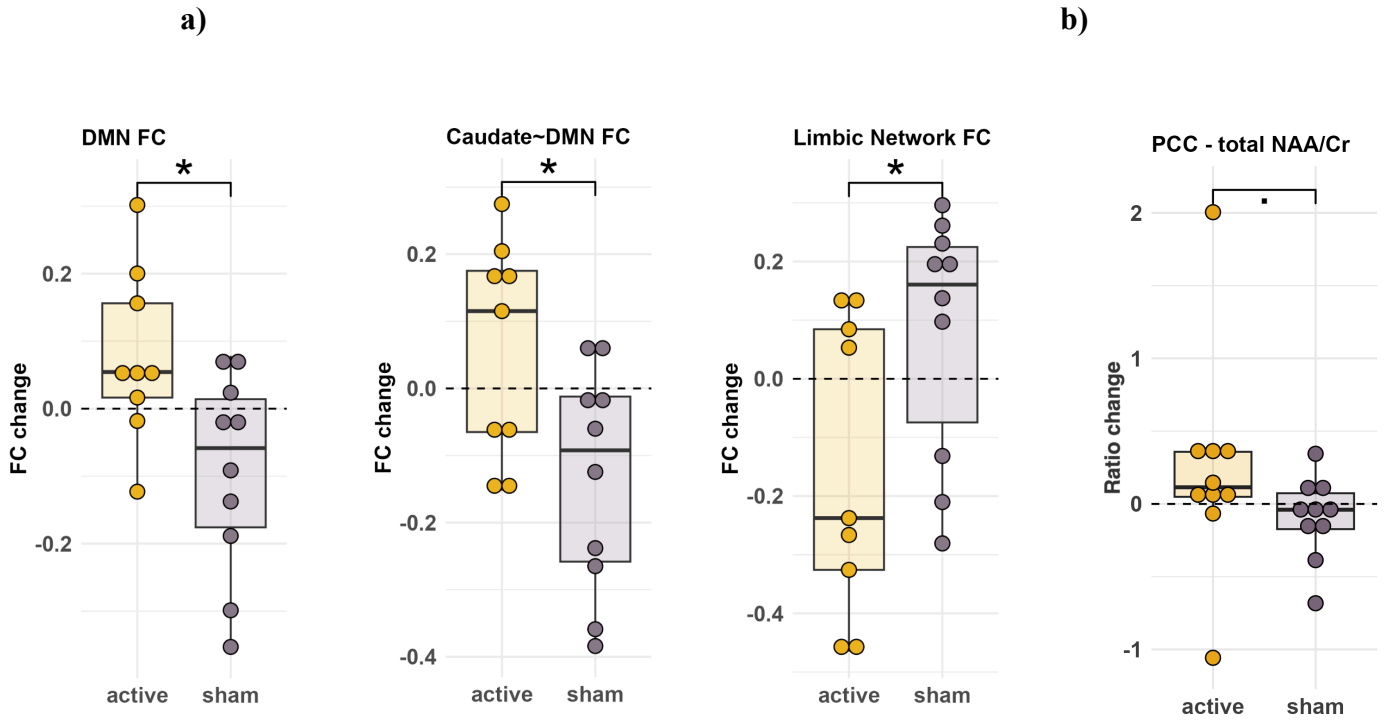

Figure 4. a) Functional Connectivity Changes with Resting-State fMRI, b) Neurometabolite ratio change in Response to tPBM

Structural MRI - T1-weighted imaging (n = 9 active, n = 9 sham)

Left nucleus accumbens volume increased by 26.6 ± 28.3 mm³ in active but decreased by –15.7 ± 40.1 mm³ in sham (t(16) = –2.59, p = 0.021, d = 1.22; Wilcoxon W = 11, Z = –2.60, p = 0.008). Right thalamic volume increased by 98.1 ± 125.2 mm³ in active versus decreased by –6.8 ± 60.5 mm³ in sham (t(16) = 2.26, p = 0.044, d = 1.07; Wilcoxon W = 18, Z = –1.99, p = 0.050).

Cortical thickness increased significantly in three regions following active tPBM compared to sham. In the right frontal pole, thickness increased in the active group by 0.0221 ± 0.0518 mm versus a decrease of 0.0347 ± 0.0409 mm in the sham group (t(16) = 2.58, p = 0.021, d = 1.22). In the right entorhinal cortex, thickness increased by 0.0659 ± 0.1069 mm in active versus a −0.0372 ± 0.0648 mm change in sham (t(16) = 2.47, p = 0.028, d = 1.17). The right pericalcarine gyrus thickness also increased in active (+0.0068 ± 0.0387 mm) but decreased in sham (−0.0348

± 0.0343 mm; t(16) = 2.41, p = 0.029, d = 1.14) (Figure 5).

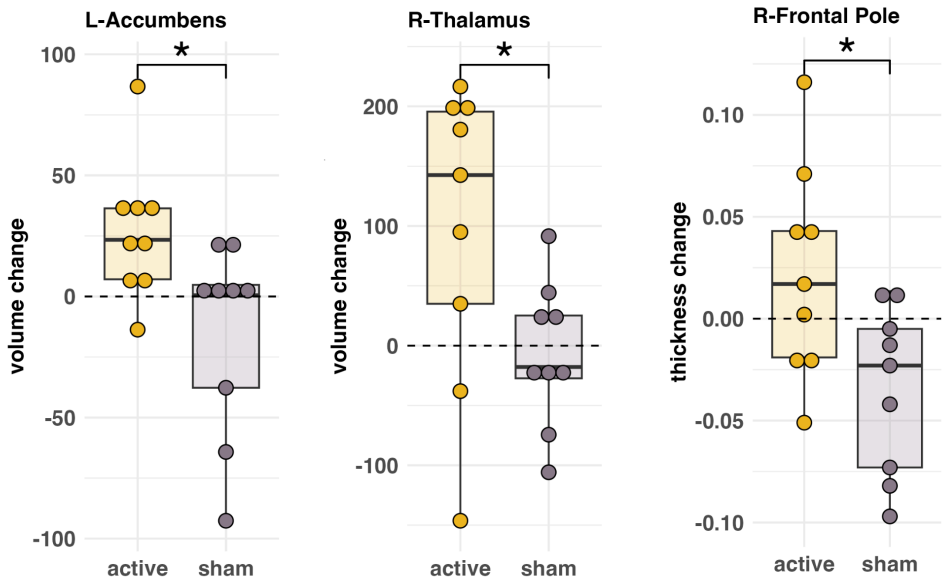

Figure 5. Structural Brain Changes in Response to tPBM

Arterial Spin Labeling (n = 9 active, n = 9 sham)

No significant differences in cerebral blood flow (CBF) were observed between the active and sham groups.

Discussion

This study is the first randomized, sham-controlled trial to evaluate the effects of transcranial photobiomodulation (tPBM) in individuals with Mild Cognitive Impairment (MCI) using a multimodal framework that integrates cognitive, blood-based metabolic —which cross the blood–brain barrier or tightly mirror central levels— and neuroimaging biomarkers. tPBM was associated with greater gains in global cognition (MMSE) and episodic memory (CVLT-II delayed recognition) compared to the sham group, along with peripheral shifts in mitochondrial-related metabolites, including increased serum pyruvate and lactate, and a reduced lactate-to-pyruvate ratio. Additionally, functional connectivity (FC) within the default mode

network (DMN) increased in the active group, suggesting enhanced network-level brain function.

The primary outcome was improvement in cognitive function. Global cognition improved significantly on the MMSE in the active group, inline with other studies[30]. The mean gain exceeded the 1- to 3-point threshold which is considered clinically meaningful[31]. Episodic memory also improved on the CVLT-II long-delay recognition task, showing more hits and fewer false positives. This is an especially meaningful finding given that recognition memory deficits emerge early in the AD trajectory (e.g., MCI)[32,33].

Blood-based metabolic markers pointed to a parallel bioenergetic shift in the active tPBM group vs. sham. Serum pyruvate increased more than lactate leading to a reduced lactate-to-pyruvate (L/P) ratio, signalling a move toward oxidative phosphorylation through the tricarboxylic acid (TCA) cycle[34] and increased mitochondrial engagement[34]. Given that MCI is often characterised by elevated lactate[35], normalisation of the L/P ratio suggests partial restoration of cerebral energy metabolism. As both metabolites cross the blood–brain barrier via monocarboxylate transporters[36], their serum levels serve as accessible proxies of brain metabolic status.

Neurometabolic imaging with proton magnetic resonance spectroscopy (^{1}H-MRS) revealed a trend toward increased N-acetylaspartate to creatine ratio (NAA/Cr) in the posterior cingulate cortex (PCC). PCC is a key DMN hub and early site of degeneration in AD[28,29]. Although not statistically significant, this trend may reflect enhanced neuronal viability or mitochondrial support[37].

FC within the DMN, measured by resting-state fMRI, increased in the active tPBM group, suggesting that tPBM may enhance communication between brain regions critical for memory, attention, and self-referential processing. The DMN was selected *a priori* due to its central role in memory and early Alzheimer's pathology[38], and its spatial overlap with tPBM stimulation sites. This finding is consistent with prior studies reporting tPBM-induced increases in DMN connectivity in MCI[27].

The absence of significant change in brain blood flow, as measured by pseudo-continuous arterial spin labeling (PCASL), aligns with previous null findings in healthy adults[39]. Transient or

subtle perfusion effects may have been missed due to the pre–post design or limited sensitivity of the acquisition sequence[40].

Our exploratory endpoints revealed several systemic and brain-level effects of tPBM. Metabolically, active tPBM modulated serum markers linked to nitrogen and one-carbon metabolism. Elevated L-alanine may reflect increased pyruvate transamination[41], while higher L-carnitine suggests enhanced mitochondrial import of fatty acids, favoring β-oxidation[42]. Reductions in urea and sarcosine point to decreased amino acid catabolism[43] with possible effects on NMDA receptor signaling[44]. Lower glycerol levels may indicate reduced lipolysis or decreased reliance on peripheral lipid stores[45]. Together, these serum metabolite shifts likely reflect improved brain energy metabolism. Alongside increased pyruvate and lactate and a reduced lactate-to-pyruvate ratio, the pattern suggests that tPBM promotes aerobic ATP production, efficient substrate handling, and metabolic homeostasis.

Active tPBM also lowered plasma IL-6– a cytokine implicated in systemic inflammation and AD progression[46]. This aligns with in vitro evidence showing PBM-mediated suppression of IL-6 and IL-8 at higher doses, and with clinical trials reporting PBM-induced reductions in IL-6, IL-8, and TNF-α in patients with COVID-19[47]. These findings support the hypothesis that tPBM may attenuate inflammation via mitochondrial mechanisms[48].

Exploratory analysis of rs-fMRI data, showed increased FC between the caudate nucleus and DMN, and decreased FC within the limbic network. The former may reflect enhanced network integration related to memory and cognitive control[49,50], while the latter may signal reduced emotional reactivity—a feature often elevated in early AD[51].

Structural MRI showed greater volume increases in the active tPBM vs sham in the left nucleus accumbens and right thalamus— subcortical regions involved in motivation, attention, and executive function that undergo early atrophy in AD[52,53]. These changes parallel findings from other neuromodulatory interventions, such as cognitive training[54] and repetitive transcranial magnetic stimulation (rTMS)[55]. In addition, modest increases in cortical thickness were also observed in the right frontal pole and right entorhinal cortex—regions implicated in working memory[56] and episodic memory[57], and among the earliest affected in AD[57]. These region-specific effects may reflect subtle structural plasticity, warranting further investigation.

A unique feature of our protocol was intranasal LED stimulation targeting the olfactory bulb—an early site of AD pathology[58,59]. Though speculative, this route may influence subcortical and limbic circuits via olfactory projections[60], potentially amplifying downstream neuromodulatory effects. Notably, the olfactory bulb, entorhinal cortex, frontal pole, nucleus accumbens, and thalamus form a functionally interconnected network involved in memory, motivation, and executive function[61]— domains impacted early in AD[62]. The structural and functional changes observed in these regions may reflect convergent tPBM effects on this distributed neurocircuitry.

Mechanistic synthesis of findings

In summary, the current study provides preliminary evidence that tPBM may modulate cognitive function and physiological processes relevant to the early stages of neurodegenerative disease. Our findings suggest that tPBM enhances mitochondrial bioenergetics, as indicated by increased serum pyruvate and lactate levels, a reduced lactate-to-pyruvate ratio, elevated L-carnitine and L-alanine, and decreased concentrations of urea, glycerol, and sarcosine. These shifts are consistent with more efficient oxidative metabolism and reduced reliance on amino acid and lipid catabolism. A concurrent reduction in plasma IL-6 further suggests potential anti-inflammatory effects. In parallel, increased functional connectivity within the DMN points to enhanced stability in memory-related brain circuits. Additionally, we speculate that the intranasal LED component may contribute to these effects by reaching deep brain structures through the olfactory bulb, which is uniquely accessible via the nasal cavity due to the absence of intervening bone. This pathway may allow light to engage limbic and subcortical regions more directly, complementing transcranial stimulation. Taken together, these results support a model in which tPBM promotes cognitive improvement by modulating mitochondrial and immunometabolic pathways that influence large-scale brain networks.

Strength & Limitations

This study is the first randomized, sham-controlled trials to evaluate tPBM in individuals with MCI, integrating cognitive assessments with blood-based and multimodal neuroimaging biomarkers. The use of a comprehensive metabolomics and inflammatory panel allowed for a multidimensional evaluation of mitochondrial and systemic effects, with pre-specified targets providing mechanistic insight. This integrative framework enabled a multidimensional

evaluation of tPBM's biological effects. Finally, high adherence rates and the use of visually indistinguishable sham devices further support the feasibility, scalability, and internal validity of home-based neuromodulation in this population.

Limitations include the small sample size (n = 10 per group), which limited power and precluded correction for multiple comparisons. The single-blind design and involvement of a single coordinator may have introduced bias. No PET or CSF biomarkers were included to confirm AD pathology. Although the design captured sustained pre–post effects, it did not assess treatment durability over time post study. Findings should be considered preliminary and hypothesis-generating.

Conclusion

This feasibility trial demonstrates that home-based tPBM is safe, well-tolerated, and shows preliminary efficacy across cognitive and biomarker outcomes in individuals with MCI. These data support the plausibility of a noninvasive, mitochondrial-targeted intervention to modulate brain structure, connectivity, and systemic metabolism. As anti-amyloid agents like lecanemab enter clinical use, therapies such as tPBM may offer additive benefit by addressing non-amyloid targets. In sum, tPBM may represent a promising candidate for noninvasive, mechanism-based intervention in early AD. Larger, double-blind, multicenter trials with longitudinal cognitive endpoints are warranted to confirm therapeutic potential.

Acknowledgement

We gratefully acknowledge TDRA-MITO2i for awarding a fellowship to the first author, and Temerty-Tanz-TDRA for their seed funding, which enabled the inception of this work. We also thank Hilary and Galen Weston Foundation for generously funding the study. We are grateful to Janine Liburd and Genane Loheswaran for their technical support and assistance in responding to device-related questions throughout the trial.

Data Availability

The data that support the findings of this study are available from the corresponding author upon reasonable request.

Code Availability

Code for statistical analyses and figure generation, including all data processing scripts, is available at: https://github.com/NedaRR/PBMCI_notebook.git. Code for the MRI processing supporting this study is available from the corresponding author upon request.

Contributions

NRR conceived and designed the study, obtained ethics approval, conducted cognitive assessments; processed MRI data, performed all statistical analyses for cognitive, blood-biomarker and MRI data; created the figures and wrote the manuscript.
NWC optimised MRI sequences, provided processing pipelines for resting-state fMRI and arterial spin labelling, and reviewed the manuscript. MJ centrifuged and aliquoted blood samples, performed Ella assays, and reviewed the manuscript. RS supported Quanterix plasma biomarker assays, and reviewed the manuscript. RZ provided photobiomodulation expertise, assisted with methodological design, and reviewed the manuscript. OR supported the Ella assays and reviewed the manuscript. ACA advised on mitochondrial assays, contributed to data interpretation, and reviewed the manuscript. TAS supported MRI acquisition and data-processing workflow and reviewed the manuscript. TKR, SJG, DGM, and LF provided scientific guidance and reviewed the manuscript. LL supplied photobiomodulation devices, and reviewed the manuscript. CEF co-designed the study, recruited participants, supervised trial conduct, and reviewed the manuscript (corresponding author).

Competing interests

NRR has received consulting fees from Vielight Inc. (2021 – 2023). RZ has received consulting fees from Vielight Inc. (2018 – present). RS holds the Elizabeth S. Barford Early Career Professor in Multiple Sclerosis in the Department of Medicine at the University of Toronto. He has received a Discovery Grant from MS Canada and additional funding from Brain Canada to study the effects of Epstein-Barr Virus on Multiple Sclerosis. He has received consulting fees

from Novartis and EMD Serono and payments or honoraria for lectures, presentations, and educational events from Biogen-Idec, Sanofi-Genzyme, EMD Serono, Roche and Eli Lilly. RS has participated on advisory boards for Novartis and EMD Serono. He has also received support for attending scientific meetings from EMD Serono. LL is the Chief Executive Officer of Vielight Inc. CEF has received research grants from Hoffmann-La Roche (2018 – 2022), Vielight Inc. (2019 – 2023) and Novo Nordisk (2021 – 2024). All other authors declare no competing interests. The remaining authors declare no competing interests.

References

1. Dementia. https://www.who.int/news-room/fact-sheets/detail/dementia.
2. Sperling, R. A. *et al.* Toward defining the preclinical stages of Alzheimer's disease: recommendations from the National Institute on Aging-Alzheimer's Association workgroups on diagnostic guidelines for Alzheimer's disease. *Alzheimers. Dement.* **7**, 280–292 (2011).
3. van Dyck, C. H. *et al.* Lecanemab in Early Alzheimer's Disease. *N. Engl. J. Med.* **388**, 9–21 (2023).
4. Cummings, J. *et al.* Lecanemab: Appropriate Use Recommendations. *J Prev Alzheimers Dis* **10**, 362–377 (2023).
5. Livingston, G. *et al.* Dementia prevention, intervention, and care: 2024 report of the Lancet standing Commission. *Lancet* **404**, 572–628 (2024).
6. 2024 Alzheimer's disease facts and figures. *Alzheimers. Dement.* **20**, 3708–3821 (2024).
7. Ward, A., Tardiff, S., Dye, C. & Arrighi, H. M. Rate of conversion from prodromal Alzheimer's disease to Alzheimer's dementia: a systematic review of the literature. *Dement. Geriatr. Cogn. Dis. Extra* **3**, 320–332 (2013).
8. Nasb, M., Tao, W. & Chen, N. Alzheimer's Disease Puzzle: Delving into Pathogenesis Hypotheses. *Aging Dis* **15**, 43–73 (2024).

9. Zhu, X.-H. *et al.* Quantitative imaging of energy expenditure in human brain. *Neuroimage* **60**, 2107–2117 (2012).

10. Mary, A., Eysert, F., Checler, F. & Chami, M. Mitophagy in Alzheimer's disease: Molecular defects and therapeutic approaches. *Mol. Psychiatry* **28**, 202–216 (2023).

11. Hirai, K. *et al.* Mitochondrial abnormalities in Alzheimer's disease. *J. Neurosci.* **21**, 3017–3023 (2001).

12. Chen, W., Zhao, H. & Li, Y. Mitochondrial dynamics in health and disease: mechanisms and potential targets. *Signal Transduct Target Ther* **8**, 333 (2023).

13. Weinrich, T. W. *et al.* A day in the life of mitochondria reveals shifting workloads. *Sci. Rep.* **9**, 13898 (2019).

14. Manczak, M. *et al.* Mitochondria are a direct site of A beta accumulation in Alzheimer's disease neurons: implications for free radical generation and oxidative damage in disease progression. *Hum. Mol. Genet.* **15**, 1437–1449 (2006).

15. Fang, E. F. *et al.* Mitophagy inhibits amyloid-β and tau pathology and reverses cognitive deficits in models of Alzheimer's disease. *Nat. Neurosci.* **22**, 401–412 (2019).

16. Cummings, J. *et al.* Alzheimer's disease drug development pipeline: 2023. *Alzheimers. Dement.* **9**, e12385 (2023).

17. Hennessy, M. & Hamblin, M. R. Photobiomodulation and the brain: a new paradigm. *J. Opt.* **19**, 013003 (2017).

18. Kolyva, C. *et al.* Systematic investigation of changes in oxidized cerebral cytochrome c oxidase concentration during frontal lobe activation in healthy adults. *Biomed Opt Express* **3**, 2550–2566 (2012).

19. Hamblin, M. R. Mechanisms and Mitochondrial Redox Signaling in Photobiomodulation.

Photochem. Photobiol. **94**, 199–212 (2018).

20. Wang, R. *et al.* Photobiomodulation for Global Cerebral Ischemia: Targeting Mitochondrial Dynamics and Functions. *Mol. Neurobiol.* **56**, 1852–1869 (2019).
21. Chang, S.-Y. & Lee, M. Y. Photobiomodulation of Neurogenesis through the Enhancement of Stem Cell and Neural Progenitor Differentiation in the Central and Peripheral Nervous Systems. *Int. J. Mol. Sci.* **24**, (2023).
22. De Taboada, L. *et al.* Transcranial laser therapy attenuates amyloid-β peptide neuropathology in amyloid-β protein precursor transgenic mice. *J. Alzheimers. Dis.* **23**, 521–535 (2011).
23. Grillo, S. L., Duggett, N. A., Ennaceur, A. & Chazot, P. L. Non-invasive infra-red therapy (1072 nm) reduces β-amyloid protein levels in the brain of an Alzheimer's disease mouse model, TASTPM. *J. Photochem. Photobiol. B* **123**, 13–22 (2013).
24. Purushothuman, S. *et al.* Near infrared light mitigates cerebellar pathology in transgenic mouse models of dementia. *Neurosci. Lett.* **591**, 155–159 (2015).
25. Baik, J. S. *et al.* Effects of Photobiomodulation on Changes in Cognitive Function and Regional Cerebral Blood Flow in Patients with Mild Cognitive Impairment: A Pilot Uncontrolled Trial. *J Alzheimers Dis* **83**, 1513–1519 (2021).
26. Saltmarche, A. E., Naeser, M. A., Ho, K. F., Hamblin, M. R. & Lim, L. Significant Improvement in Cognition in Mild to Moderately Severe Dementia Cases Treated with Transcranial Plus Intranasal Photobiomodulation: Case Series Report. *Photomed Laser Surg* **35**, 432–441 (2017).
27. Chao, L. L. Effects of Home Photobiomodulation Treatments on Cognitive and Behavioral Function, Cerebral Perfusion, and Resting-State Functional Connectivity in Patients with

Dementia: A Pilot Trial. *Photobiomodul Photomed Laser Surg* **37**, 133–141 (2019).

28. Garcia-Garcia, D. *et al.* Posterior parietooccipital hypometabolism may differentiate mild cognitive impairment from dementia in Parkinson's disease. *Eur J Nucl Med Mol Imaging* **39**, 1767–1777 (2012).
29. Huang, M. *et al.* A comparative study of posterior cingulate metabolism in patients with mild cognitive impairment due to Parkinson's disease or Alzheimer's disease. *Sci Rep* **13**, 14241 (2023).
30. Papi, S. *et al.* The effect of transcranial photobiomodulation on cognitive function and attentional performance of older women with mild cognitive impairment: a randomized controlled trial. *Prz Menopauzalny* **21**, 157–164 (2022).
31. Lansdall, C. J. *et al.* Establishing Clinically Meaningful Change on Outcome Assessments Frequently Used in Trials of Mild Cognitive Impairment Due to Alzheimer's Disease. *J Prev Alzheimers Dis* **10**, 9–18 (2023).
32. Bennett, I. J., Golob, E. J., Parker, E. S. & Starr, A. Memory evaluation in mild cognitive impairment using recall and recognition tests. *J. Clin. Exp. Neuropsychol.* **28**, 1408–1422 (2006).
33. Wolk, D. A., Signoff, E. D. & Dekosky, S. T. Recollection and familiarity in amnestic mild cognitive impairment: a global decline in recognition memory. *Neuropsychologia* **46**, 1965–1978 (2008).
34. Bouzier-Sore, A.-K., Voisin, P., Canioni, P., Magistretti, P. J. & Pellerin, L. Lactate is a preferential oxidative energy substrate over glucose for neurons in culture. *J. Cereb. Blood Flow Metab.* **23**, 1298–1306 (2003).
35. Zebhauser, P. T. *et al.* Cerebrospinal fluid lactate levels along the Alzheimer's disease

continuum and associations with blood-brain barrier integrity, age, cognition, and biomarkers. *Alzheimers Res Ther* **14**, 61 (2022).

36. Gonzalez, S. V., Nguyen, N. H. T., Rise, F. & Hassel, B. Brain metabolism of exogenous pyruvate. *J. Neurochem.* **95**, 284–293 (2005).
37. Moffett, J. R., Ross, B., Arun, P., Madhavarao, C. N. & Namboodiri, A. M. A. N-Acetylaspartate in the CNS: from neurodiagnostics to neurobiology. *Prog Neurobiol* **81**, 89–131 (2007).
38. Ereira, S., Waters, S., Razi, A. & Marshall, C. R. Early detection of dementia with default-mode network effective connectivity. *Nat. Ment. Health* **2**, 787–800 (2024).
39. Spera, V. *et al.* Pilot Study on Dose-Dependent Effects of Transcranial Photobiomodulation on Brain Electrical Oscillations: A Potential Therapeutic Target in Alzheimer's Disease. *J Alzheimers Dis* **83**, 1481–1498 (2021).
40. Kaneta, T. *et al.* Head-to-Head Visual Comparison between Brain Perfusion SPECT and Arterial Spin-Labeling MRI with Different Postlabeling Delays in Alzheimer Disease. *AJNR Am J Neuroradiol* **38**, 1562–1568 (2017).
41. Sonnay, S., Gruetter, R. & Duarte, J. M. N. How Energy Metabolism Supports Cerebral Function: Insights from C Magnetic Resonance Studies. *Front Neurosci* **11**, 288 (2017).
42. Pekala, J. *et al.* L-carnitine--metabolic functions and meaning in humans life. *Curr. Drug Metab.* **12**, 667–678 (2011).
43. Holeček, M. Branched-chain amino acids in health and disease: metabolism, alterations in blood plasma, and as supplements. *Nutr Metab (Lond)* **15**, 33 (2018).
44. Tanas, A. *et al.* and Neuroprotective Effects of Sarcosine. *Biomed Res Int* **2022**, 5467498 (2022).

45. Robergs, R. A. & Griffin, S. E. Glycerol. Biochemistry, pharmacokinetics and clinical and practical applications. *Sports Med* **26**, 145–167 (1998).

46. Lyra E Silva, N. M. *et al.* Pro-inflammatory interleukin-6 signaling links cognitive impairments and peripheral metabolic alterations in Alzheimer's disease. *Transl Psychiatry* **11**, 251 (2021).

47. Marashian, S. M. *et al.* Photobiomodulation Improves Serum Cytokine Response in Mild to Moderate COVID-19: The First Randomized, Double-Blind, Placebo Controlled, Pilot Study. *Front Immunol* **13**, 929837 (2022).

48. Lepiarz-Raba, I., Gbadamosi, I., Florea, R., Paolicelli, R. C. & Jawaid, A. Metabolic regulation of microglial phagocytosis: Implications for Alzheimer's disease therapeutics. *Transl Neurodegener* **12**, 48 (2023).

49. Rieckmann, A., Johnson, K. A., Sperling, R. A., Buckner, R. L. & Hedden, T. Dedifferentiation of caudate functional connectivity and striatal dopamine transporter density predict memory change in normal aging. *Proc Natl Acad Sci U S A* **115**, 10160–10165 (2018).

50. Fjell, A. M. *et al.* Brain Events Underlying Episodic Memory Changes in Aging: A Longitudinal Investigation of Structural and Functional Connectivity. *Cereb Cortex* **26**, 1272–1286 (2016).

51. Benavides-Varela, S. *et al.* The role of limbic structures in financial abilities of mild cognitive impairment patients. *Neuroimage Clin* **26**, 102222 (2020).

52. van de Mortel, L. A., Thomas, R. M., van Wingen, G. A. & Alzheimer's Disease Neuroimaging Initiative. Grey Matter Loss at Different Stages of Cognitive Decline: A Role for the Thalamus in Developing Alzheimer's Disease. *J. Alzheimers. Dis.* **83**, 705–720

(2021).

53. Hari, E. *et al.* Volumetric and functional connectivity changes of the thalamic nuclei in different stages of Alzheimer's disease. *Clin. Neurophysiol.* **165**, 127–137 (2024).

54. Ramsay, I. S. *et al.* Response to Targeted Cognitive Training Correlates with Change in Thalamic Volume in a Randomized Trial for Early Schizophrenia. *Neuropsychopharmacology* **43**, 590–597 (2018).

55. Wang, Z. *et al.* Increased thalamic gray matter volume induced by repetitive transcranial magnetic stimulation treatment in patients with major depressive disorder. *Front. Psychiatry* **14**, 1163067 (2023).

56. Zacharopoulos, G., Klingberg, T. & Cohen Kadosh, R. Cortical surface area of the left frontal pole is associated with visuospatial working memory capacity. *Neuropsychologia* **143**, 107486 (2020).

57. Kulason, S. *et al.* Entorhinal and Transentorhinal Atrophy in Preclinical Alzheimer's Disease. *Front Neurosci* **14**, 804 (2020).

58. Son, G. *et al.* Olfactory neuropathology in Alzheimer's disease: a sign of ongoing neurodegeneration. *BMB Rep* **54**, 295–304 (2021).

59. Zou, Y.-M., Lu, D., Liu, L.-P., Zhang, H.-H. & Zhou, Y.-Y. Olfactory dysfunction in Alzheimer's disease. *Neuropsychiatr Dis Treat* **12**, 869–875 (2016).

60. Lu, J. *et al.* Disruptions of the olfactory and default mode networks in Alzheimer's disease. *Brain Behav* **9**, e01296 (2019).

61. Gipson, C. D., Kupchik, Y. M. & Kalivas, P. W. Rapid, transient synaptic plasticity in addiction. *Neuropharmacology* **76 Pt B**, 276–286 (2014).

62. Cloutier, S., Chertkow, H., Kergoat, M.-J., Gauthier, S. & Belleville, S. Patterns of

Cognitive Decline Prior to Dementia in Persons with Mild Cognitive Impairment. *J Alzheimers Dis* **47**, 901–913 (2015).

63. Petersen, R. C. *et al.* Mild cognitive impairment due to Alzheimer disease in the community. *Ann. Neurol.* **74**, 199–208 (2013).
64. Whitehead, A. L., Julious, S. A., Cooper, C. L. & Campbell, M. J. Estimating the sample size for a pilot randomised trial to minimise the overall trial sample size for the external pilot and main trial for a continuous outcome variable. *Stat Methods Med Res* **25**, 1057–1073 (2016).
65. Kunselman, A. R. A brief overview of pilot studies and their sample size justification. *Fertil Steril* **121**, 899–901 (2024).
66. Folstein, M. F., Folstein, S. E. & McHugh, P. R. 'Mini-mental state'. A practical method for grading the cognitive state of patients for the clinician. *J Psychiatr Res* **12**, 189–198 (1975).
67. Arnett, J. A. & Labovitz, S. S. Effect of physical layout in performance of the Trail Making Test. *Psychol. Assess.* **7**, 220–221 (1995).
68. Delis, D. C., Kramer, J. H., Kaplan, E. & Ober, B. A. California Verbal Learning Test--Second Edition. *PsycTESTS Dataset* American Psychological Association (APA) https://doi.org/10.1037/t15072-000 (2016).
69. Kramer, A. O. *et al.* Robust normative standards for the California Verbal Learning Test (CVLT) ages 60-89: A tool for early detection of memory impairment. *Clin Neuropsychol* **34**, 384–405 (2020).
70. Woods, S. P., Delis, D. C., Scott, J. C., Kramer, J. H. & Holdnack, J. A. The California Verbal Learning Test--second edition: test-retest reliability, practice effects, and reliable change indices for the standard and alternate forms. *Arch Clin Neuropsychol* **21**, 413–420

(2006).

71. Buysse, D. J., Reynolds, C. F., 3rd, Monk, T. H., Berman, S. R. & Kupfer, D. J. The Pittsburgh Sleep Quality Index: a new instrument for psychiatric practice and research. *Psychiatry Res* **28**, 193–213 (1989).

72. Ismail, Z. *et al.* The Mild Behavioral Impairment Checklist (MBI-C): A Rating Scale for Neuropsychiatric Symptoms in Pre-Dementia Populations. *J Alzheimers Dis* **56**, 929–938 (2017).

73. Psychogios, N. *et al.* The human serum metabolome. *PLoS One* **6**, e16957 (2011).

74. Saude, E. J., Slupsky, C. M. & Sykes, B. D. Optimization of NMR analysis of biological fluids for quantitative accuracy. *Metabolomics* **2**, 113–123 (2006).

75. Rout, M. *et al.* MagMet: A fully automated web server for targeted nuclear magnetic resonance metabolomics of plasma and serum. *Magn Reson Chem* **61**, 681–704 (2023).

76. Tanaka, T., Narazaki, M. & Kishimoto, T. IL-6 in inflammation, immunity, and disease. *Cold Spring Harb Perspect Biol* **6**, a016295 (2014).

77. de Brito, R. de C. C. M. *et al.* The balance between the serum levels of IL-6 and IL-10 cytokines discriminates mild and severe acute pneumonia. *BMC Pulm Med* **16**, 170 (2016).

78. Samadzadeh, S. & Sleator, R. D. The role of Neurofilament light (NfL) and glial fibrillary acidic protein (GFAP) in MS and AQP4-NMOSD: Advancing clinical applications. *eNeurologicalSci* **38**, 100550 (2025).

79. Kahn, O. I. *et al.* Secreted neurofilament light chain after neuronal damage induces myeloid cell activation and neuroinflammation. *Cell Rep* **44**, 115382 (2025).

80. Ashton, N. J. *et al.* Diagnostic Accuracy of a Plasma Phosphorylated Tau 217 Immunoassay for Alzheimer Disease Pathology. *JAMA Neurol* **81**, 255–263 (2024).

81. Bathina, S. & Das, U. N. Brain-derived neurotrophic factor and its clinical implications. *Arch Med Sci* **11**, 1164–1178 (2015).

82. Mondesert, E. *et al.* Comparative Performances of 4 Serum NfL Assays, pTau181, and GFAP in Patients With Amyotrophic Lateral Sclerosis. *Neurology* **104**, e213400 (2025).

83. Churchill, N. W. *et al.* Effects of post-acute COVID-19 syndrome on the functional brain networks of non-hospitalized individuals. *Front Neurol* **14**, 1136408 (2023).

84. Schaefer, A. *et al.* Local-Global Parcellation of the Human Cerebral Cortex from Intrinsic Functional Connectivity MRI. *Cereb Cortex* **28**, 3095–3114 (2018).

85. Tian, Y., Margulies, D. S., Breakspear, M. & Zalesky, A. Topographic organization of the human subcortex unveiled with functional connectivity gradients. *Nat Neurosci* **23**, 1421–1432 (2020).

86. Fischl, B. *et al.* Automatically parcellating the human cerebral cortex. *Cereb. Cortex* **14**, 11–22 (2004).

87. Fischl, B. & Dale, A. M. Measuring the thickness of the human cerebral cortex from magnetic resonance images. *Proc. Natl. Acad. Sci. U. S. A.* **97**, 11050–11055 (2000).

88. Desikan, R. S. *et al.* An automated labeling system for subdividing the human cerebral cortex on MRI scans into gyral based regions of interest. *Neuroimage* **31**, 968–980 (2006).

89. Churchill, N. W., Hutchison, M. G., Graham, S. J. & Schweizer, T. A. Post-Concussion Brain Changes Relative to Pre-Injury White Matter and Cerebral Blood Flow: A Prospective Observational Study. *Neurology* **104**, e213374 (2025).

90. Wang, Z. *et al.* Empirical optimization of ASL data analysis using an ASL data processing toolbox: ASLtbx. *Magn Reson Imaging* **26**, 261–269 (2008).

91. Permutation inference for the general linear model. *NeuroImage* **92**, 381–397 (2014).